Chemical Science

EDGE ARTICLE

View Article Online
View Journal | View Issue

Cite this: *Chem. Sci.*, 2018, **9**, 6292

Similar ligand–metal bonding for transition metals and actinides? $5f^1$ $U(C_7H_7)_2^-$ *versus* $3d^n$ metallocenes†

Dumitru-Claudiu Sergentu, Frédéric Gendron and Jochen Autschbach *

$U(C_7H_7)_2^-$ is a fascinating $5f^1$ complex whose metal–ligand bonding was assigned in the literature as being very similar to $3d^7$ cobaltocene, based on a crystal-field theoretical interpretation of the experimental magnetic resonance data. The present work provides an in-depth theoretical study of the electronic structure, bonding, and magnetic properties of the $5f^1$ $U(C_7H_7)_2^-$ *vs.* 3d metallocenes with V, Co, and Ni, performed with relativistic wavefunction and density functional methods. The ligand to metal donation bonding in $U(C_7H_7)_2^-$ is strong and in fact similar to that in vanadocene, in the sense that the highest occupied arene orbitals donate electron density into empty metal orbitals of the same symmetry with respect to the rotational axis ($3d_\pi$ for V, $5f_\delta$ for U), but selectively with α spin (↑). For Co and Ni, the dative bonding from the ligands is β spin (↓) selective into partially filled $3d_\pi$ orbitals. In all systems, this spin delocalization triggers spin polarization in the arene σ bonding framework, causing proton spin densities opposite to those of the carbons. As a consequence, the proton spin densities and hyperfine coupling constants $A_{iso}^{^1H}$ are negative for the Co and Ni complex, but positive for vanadocene. The $A_{iso}^{^1H}$ of $U(C_7H_7)_2^-$ is negative and similar to that of cobaltocene, but only because of the strong spin–orbit coupling in the actinocene, which causes $A_{iso}^{^1H}$ to be opposite to the sign of the proton spin density. The study contributes to a better understanding of actinide 5f *vs.* transition metal 3d covalency, and highlights potential pitfalls when interpreting experimental magnetic resonance data in terms of covalent bonding for actinide complexes.

Received 18th December 2017
Accepted 10th June 2018

DOI: 10.1039/c7sc05373h

rsc.li/chemical-science

1 Introduction

Metal sandwich complexes are an important class of organometallic compounds and have attracted the attention of theoreticians and experimentalists for many decades.[1–4] These compounds feature a metal center between two (nearly) parallel arene ligands, usually in highly symmetric structures. The metal ion can be a low oxidation-state transition metal (TM), a lanthanide (Ln), or an actinide (An). Common metallocenes are the $TM(C_5H_5)_2$, where a TM^{2+} ion is sandwiched between two cyclopentadienyl ligands. This series debuted with the discovery of ferrocene (TM = Fe)[5–8] in the 1950s, and new members were synthesized soon after. Common lanthanocenes and actinocenes are the bis[8]annulene complexes $M(C_8H_8)_2$ (M = Ac or Ln).[9–15] Cerocene (Ln = Ce) and uranocene (Ac = U) are two well-studied examples from these series, the former because of the mixed-valence oxidation state of the Ce center (III+ *vs.* IV+),[16–21] and the later because of the central role that U plays in the development of organoactinide chemistry.[15,22–25] The set of known U-based sandwich complexes also includes the unusual $U(C_7H_7)_2^-$ (a uranocene analogue).[26–28] It has been debated whether the oxidation state of U in this compound is +III or +V. The +V oxidation state corresponds to U-$5f^1$ and is supported by magnetic measurements and crystal-field (CF) analyses,[27,28] while a III+ oxidation state corresponds to U-$5f^3$ and can be justified by the strong metal–ligand bonding in the complex.[28] Therefore, the metal center in $U(C_7H_7)_2^-$ can be regarded as formally $5f^3$ U^{III}, or $5f^1$ U^V with substantial ligand to metal donation bonding. We note that the assigned formal oxidation state and the actual metal charge may be different.

The lanthanocenes and actinocenes are of fundamental interest in chemistry, because of the varying degree of the involvement of the heavy metal orbitals in bonding interactions *via* their 4f–5d and 5f–6d shells, respectively.[15,24,29–32] It is important to distinguish the symmetry of the frontier arene π orbitals with respect to the principal symmetry axis of the sandwich compound. In the following, we use subscripts σ, π, δ, ϕ for $|m_\ell| = 0, 1, 2, 3$, such that, for instance, π_δ denotes a π orbital of an arene ligand that has a δ nodal pattern with respect to the principal axis of the complex and can overlap with a metal $3d_\delta$ or $5f_\delta$ orbital.

Department of Chemistry, University at Buffalo, State University of New York, Buffalo, NY 14260-3000, USA. E-mail: jochena@buffalo.edu

† Electronic supplementary information (ESI) available: Additional support material comprising atomic spin populations, scans of potential energy surfaces and various CAS(PT2)-SR(SO) data. See DOI: 10.1039/c7sc05373h

Metal–ligand interactions are already complex in TM metallocenes, as evidenced in early studies,[1,33–40] and perhaps even more so in actinocenes.[24,30,31] The complexity arises from a number of factors: ligand-to-metal (L–M) donation and metal-to-ligand (M–L) back-donation may take place, the L–M and M–L interactions may have preference for α spin (↑) over β spin (↓), or *vice versa*, if the metal ion has unpaired spins, valence electrons may be distributed among d and/or f metal-centered orbitals such that multi-configurational electronic ground-states (GSs) and low-energy excited states (ESs) arise, and there may be non-vanishing orbital angular momenta in addition to the electron spin angular momenta. The picture gets complicated further by spin polarization effects, and by relativistic effects. Spin–orbit coupling (SOC), in particular, becomes very large in actinide complexes while at the same time the comparatively large radial extension of the An 5f shell gives rise to a 5f ligand field (LF) that is much stronger than for the lanthanide 4f shell. As a consequence, for actinides, 5f, along with 6d and 7s, may participate in covalent bonding.[31] The complicated interplay of these interactions renders experimental magnetic resonance data, for instance, difficult to interpret without theoretical support.

Interestingly, there are experimental findings that point to rather similar ligand–metal bonding in the aforementioned systems $U(C_7H_7)_2^-$ and $Co(C_5H_5)_2$. In the remainder of this work, $U(C_7H_7)_2^-$ will be considered to exhibit a $5f^1$ metal center to underline the metal unpaired 5f electron count. In any case, the assigned formal metal oxidation state, being either III or V, has no bearing on the actual electron (spin) density in $U(C_7H_7)_2^-$. In a seminal article, Gourier *et al.*[27] reported experimental condensed-phase magnetic resonance data for $U(C_7H_7)_2^-$. Based on a CF model, Gourier *et al.* predicted *g* factors in agreement with the experiment and concluded that the GS of $U(C_7H_7)_2^-$ is predominantly $5f_\pi$ in character (51.4%) with an important admixture of $5f_\sigma$ (38.5%), as dictated by the combined influence of SOC and CF effects, and minor contributions from $5f_\phi$ and $5f_\delta$. A sizable negative isotropic ^{1}H hyperfine coupling constant (HyFCC), $A_{iso}^{^1H} = -2.7$ MHz, was interpreted as indicating negative spin density, *i.e.* an excess of β-spin (↓) *versus* α-spin (↑) density, at the arene protons in $U(C_7H_7)_2^-$, triggered by a positive spin density (excess ↑) at the C centers and the McConnell spin polarization mechanism.[34] In turn, the positive carbon spin density was thought to be caused by β-spin donation from the arene π_σ and π_π orbitals into the half-filled U orbitals of mixed $5f_\sigma$–$5f_\pi$ character. On the basis of the sign and magnitude of $A_{iso}^{^1H}$ and estimated spin density of $\rho^{\alpha-\beta} \geq 0.036$ in the individual C_{2p_z} orbitals, and their similarity with cobaltocene ($A_{iso}^{^1H} = -2.4$ MHz and $\rho^{\alpha-\beta} \geq 0.078$),[41] Gourier *et al.* concluded that extensive covalent ligand–metal bonding must be present in $U(C_7H_7)_2^-$, and that it is similar to the bonding $Co(C_5H_5)_2$ as far as the spin density is concerned.

The apparent similarity of the metal–ligand bonding in these two systems is very intriguing, because the interaction between the Co 3d and U 5f orbitals with the ligand orbitals is expected to be quite different already at the scalar relativistic (SR) level of theory,[28,29,41] *i.e.* without considering SOC. For instance, the highest occupied arene frontier orbital, interacting most strongly with the metal, is π_π for $C_5H_5^-$ but π_δ for $C_7H_7^{3-}$, as correctly noted by Gourier *et al.* The SOC is expected to complicate the bonding picture for the $U(C_7H_7)_2^-$ further, while it does not play a significant role for cobaltocene or other TM metallocenes. The overall spin density distribution in the two sandwich complexes, and the underlying bonding mechanisms, may therefore be very different. This would mean, however, that a similar $A_{iso}^{^1H}$ for cobaltocene and the $5f^1$ $U(C_7H_7)_2^-$ is caused by a mechanism that was not taken into consideration previously. For instance, the observed sign for the $A_{iso}^{^1H}$ may also be due to the PSO mechanism (paramagnetic interaction of the nuclear spin with the electron orbital angular momentum). PSO contributes to the hyperfine coupling when there is an electron orbital angular momentum. The latter may arise from spatial degeneracies, from the SOC, or a combination thereof. For details on the PSO and other mechanisms that influence the HyFCCs, we refer the reader to a selection of specialized articles.[42–48]

Herein, the electronic structures, the chemical bonding, and the magnetic properties (*g* factors, ^{13}C and ^{1}H HyFCCs), in $U(C_7H_7)_2^-$ and $TM(C_5H_5)_2$ with TM = V, Co, and Ni are studied in detail with relativistic density functional theory (DFT) and multiconfigurational wavefunction methods. We specifically chose these three TM systems for comparison with the $U(C_7H_7)_2^-$ because they show distinct L–M and M–L interactions that translate into distinct magnetic properties.[42,49–52] It is shown that the L–M bonding in $U(C_7H_7)_2^-$ is in fact quite similar to that in vanadocene, triggering positive spin densities at the ligand protons. However, when SOC is accounted for, the proton HyFCC in $U(C_7H_7)_2^-$ has a negative sign and is similar in value to that of cobaltocene, even though cobaltocene has negative spin density at the protons and different ligand to metal donation bonding. The findings suggest that a spin–orbit induced PSO mechanism is crucial and determines the sign of the proton HyFCC in $U(C_7H_7)_2^-$.

2 Computational details

Equilibrium geometries for the $TM(C_5H_5)_2$, TM = V, Co, Ni, and $U(C_7H_7)_2^-$ systems were obtained by SR-DFT employing the Amsterdam Density Functional (ADF) package[53] and the zeroth order regular approximation (ZORA) all-electron relativistic Hamiltonian.[54] For the D_{5h} structure of $Co(C_5H_5)_2$ and an excited state of $U(C_7H_7)_2^-$, the DFT calculations were performed using an 'average-of-configuration' (AOC) fractional orbital occupation scheme to avoid symmetry breaking. Different exchange–correlation functionals, namely the BP[55,56] and PBE[57,58] generalized gradient approximations (GGAs) and the B3LYP[59–61] and PBE0 [62,63] hybrid GGAs, were used in conjunction with all-electron doubly-polarized triple-ζ (TZ2P) Slater-type basis sets.[64] Additional details of the electronic structures, *e.g.* orbital occupations, atomic spin densities, were explored *via* natural bond orbital (NBO) calculations.[65] Similar calculations were also carried at the eclipsed (D_{8h}) experimental structure with standard C–H bond lengths, of $U(C_8H_8)$ ($5f^2$ uranocene),[13,14] in order to make comparisons with the $5f^1$ $U(C_7H^7)_2^-$. If not indicated otherwise, plots of orbital isosurfaces

correspond to AOC spin-restricted open-shell calculations with a common set of α spin (↑) and β spin (↓) orbitals, while spin density plots and numerical spin populations are based on spin-unrestricted DFT calculations with separate sets of α and β spin orbitals.

With DFT, magnetic properties (*g* factors, $A_{iso}^{^{13}C}$ and $A_{iso}^{^{1}H}$) were calculated using the NMR,[66,67] CPL[68–70] and ESR[71,72] modules of ADF. In the NMR and CPL modules, the effect of SOC on the *g* and *A* matrices is introduced *via* perturbation theory on top of SR-ZORA ground states. In the ESR module, the effect of SOC is treated self-consistently *via* the use of the two-component relativistic spin–orbit (SO) ZORA Hamiltonian (SO-ZORA). For metallocenes, the SO-ZORA calculations used a spin-unrestricted formalism with collinear spin densities, to allow for spin-polarization effects in the computation of the *g* factors or HyFCCs, which are important for strong metal–ligand covalency. For $U(C_7H_7)_2^-$, the *g* factors and HyFCCs were also calculated within a SO-ZORA approach that makes use of a spin-restricted formalism. Although this restricted formalism does not allow for the evaluation of spin polarization effects, it properly imposes Kramers symmetry, which is more important for this system governed by strong SOC. The aforementioned density functionals were used in the magnetic-property calculations, in conjunction with a quadruply-polarized quadruple-ζ (QZ4P) Slater-type basis set for the metal,[64] and the 'jcpl' augmented version of TZ2P for C and H.[73]

Ab initio wave function calculations were performed using the Molcas software[74] (pre v8.1 developers' version). The complete active space self-consistent field method (CASSCF)[75] was used to introduce mostly static correlation. Dynamic correlation was treated by complete active space perturbation theory at second order (CASPT2).[76] The PT2 calculations used an imaginary shift of 0.2 and an ionization potential electron affinity shift of zero. SR effects were treated *via* the second-order Douglas–Kroll–Hess Hamiltonian[77–80] in conjunction with all-electron atomic natural orbital relativistically contracted basis sets of polarized valence triple-ζ quality (ANO-RCC-VTZP).[81–83] Various active spaces (n_{el}, m_{orb}), with n_{el} being the number of active electrons and m_{orb} number of active orbitals, were considered for the different complexes as detailed in Section S2 of the ESI.† Additional spin-polarization effects were introduced through the restricted active space configuration interaction approach (RASCI) following a scheme analyzed by Suaud *et al.*[84] (ESI, Section S2†). RASCI was previously used to treat a limited extent of spin polarization in actinide complexes.[44,45,85]

SOC was treated in a configuration interaction fashion using the restricted active space state interaction (RASSI) module[86] of Molcas. In this approach, a state-interaction matrix is constructed in the basis of the spin components of the SR CASSCF states, the diagonal elements being either CASSCF or CASPT2 energies, and off-diagonal SOC matrix elements are computed within a mean-field approximation.[87] All SOC calculations were followed by computations of *g* factors using the approach described in ref. 88 and implemented in the RASSI module of Molcas. For brevity, SR/SOC CASSCF and CASPT2 is referred as CAS-SR/CAS-SO and PT2-SR/PT2-SO in the following.

3 Results and discussion

3.1 Equilibrium structures and ground electronic spin-states

The structures of the complexes are shown in Fig. 1. As the structural features of the 3d metallocenes, and the question of an eclipsed *vs.* staggered conformation, are well known, details regarding the structure optimizations and experimental data can be found in the ESI.† For the bonding analyses and the magnetic property calculations in this study, optimized D_{5h} eclipsed conformers with a five-fold rotational axis of symmetry were used for the metallocenes with V and Ni. The 3d orbital degeneracy of the metal ions is lifted by the axial LF into a $3d_\sigma$ (a_1' in D_{5h}) and twofold degenerate $3d_\delta$ (e_2') and $3d_\pi$ (e_1'') orbitals. For vanadocene, V^{2+} ($3d^3$), the shell filling gives rise to a CF $(3d_\sigma)^1(3d_\delta)^2(3d_\pi)^0$ configuration and a spin-quartet $^4A_1'$ GS. For nickelocene, Ni^{2+} ($3d^8$), the CF configuration is $(3d_\sigma)^2(3d_\delta)^4(3d_\pi)^2$ and the GS is a spin-triplet $^3A_1'$. Note that the 3d-shell occupations are confirmed by experiments for both vanadocene[89–91] and nickelocene.[89,90,92]

Cobaltocene affords a Co^{2+} ($3d^7$) ion with a formal $(3d_\sigma)^2(3d_\delta)^4(3d_\pi)^1$ CF configuration.[90,93] The unpaired electron in the degenerate $3d_\pi$ orbitals leads to an orbitally degenerate spin-doublet GS, $^2E_1''$ in D_{5h} symmetry. Jahn–Teller (JT) distortions[94,95] remove the orbital-degeneracy by symmetry lowering to C_{2v}, leading to a spin-doublet GS of $^2B_1$ symmetry.[49,93,96] The structure affords three types of symmetry-unique C atoms (Fig. 1), which are on average ~2.10 Å away from the Co center (BP/TZ2P, Table S1†). Irrespective of the used functional, the structural parameters of the optimized JT geometry are similar to the ones found for the five-fold symmetric structures because the magnitude of the JT distortion is small. The optimized BP/TZ2P C_{2v} JT structure was used for subsequent calculations, unless specified otherwise.

For $U(C_7H_7)_2^-$, the axial LF lifts the 5f degeneracy into a $5f_\sigma$ (a_2'' in the D_{7h} eclipsed structure), and pairs of twofold degenerate $5f_\phi$ (e_3'), $5f_\pi$ (e_1') and $5f_\delta$ (e_2'') orbitals. In a SR theoretical description, the unpaired electron occupies the $5f_\sigma$ orbital, giving rise to a spin-doublet electronic GS of $^2A_2''$.[28] The optimized SR geometry (see Table S1†) is in good agreement with the experimental condensed phase X-ray diffraction (XRD) data.

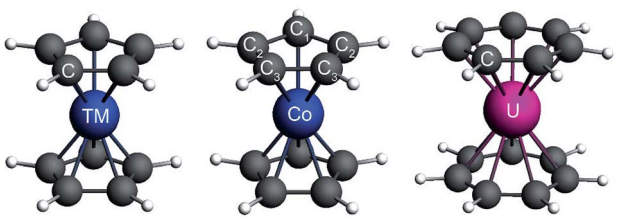

Fig. 1 Balls & sticks representations of the optimized structures of V and Ni metallocene (left), $Co(C_5H_5)_2$ (center, JT distorted structure), and the averaged XRD structure of $U(C_7H_7)_2^-$ (right). Light grey corresponds to hydrogen atoms.

This suggests that structural changes due to SOC are insignificant. The SR GS of $U(C_7H_7)_2^-$ is orbitally non-degenerate and therefore it does not undergo JT distortions. On experimental grounds however, due to crystal packing, the solid state structure exhibits a lower C_{2h} symmetry,[26] with U–C distances that agree within 0.1 Å. Since the distortion is small, a D_{7h} geometry with averaged experimental U–C and C–C distances and BP/TZ2P optimized H positions ('averaged experimental structure') was used for subsequent calculations.

3.2 Electronic structures and metal–ligand bonding from DFT calculations

In the LF molecular orbital (MO) picture, the metal orbitals may form in-phase bonding and out-of-phase antibonding linear combinations with ligand orbitals of matching symmetry, which facilitates the important L–M donation bonding and M–L back-donation. Frontier MO diagrams for the eclipsed TM metallocenes and $U(C_7H_7)_2^-$ are shown in Fig. 2, along with isosurfaces of relevant calculated orbitals.

3.2.1 Metallocenes. In the TM metallocenes considered herein, the metal $3d_\sigma$ orbitals remain formally nonbonding in the molecules. The M–L back-bonding interactions between the $3d_\delta$ metal and empty arene π_δ orbitals are moderately strong, resulting in two pairs of twofold degenerate $(\pi_\delta–3d_\delta)_\pm$ MOs of bonding (+, filled or half occupied) and antibonding (−, empty) character. The $(\pi_\delta–3d_\delta)_+$ MOs remain predominantly metal-centered. The $3d_\pi$ TM orbitals strongly interact with the filled arene π_π orbitals, generating twofold degenerate $(\pi_\pi–3d_\pi)_\pm$ MOs with pronounced bonding (+) and antibonding (−) character, respectively. The $(\pi_\pi–3d_\pi)_-$ combinations correspond formally to the metal $3d_\pi$ orbitals in CF theory, but they exhibit substantial mixing with the ligands.

In the investigated TM metallocenes, most of the spin density is localized on the metal centers, as expected (Tables S3 and S4† and Fig. 3). Spin density in the ligands is caused by spin-delocalization, due to spin-selective L–M donation and/or spin-selective M–L back-donation, and 'fine-tuned' by spin polarization effects,[42,97,98] as shown in Fig. 4. For example, a previous study showed that for nickelocene a positive spin density, *i.e.* an excess of α spin, around the carbons and at the carbon nuclei, as quantified experimentally by paramagnetic effects on the NMR shifts, is caused to *ca.* 85% by β spin L–M donation and to 15% by M–L α spin delocalization.[42] Spin

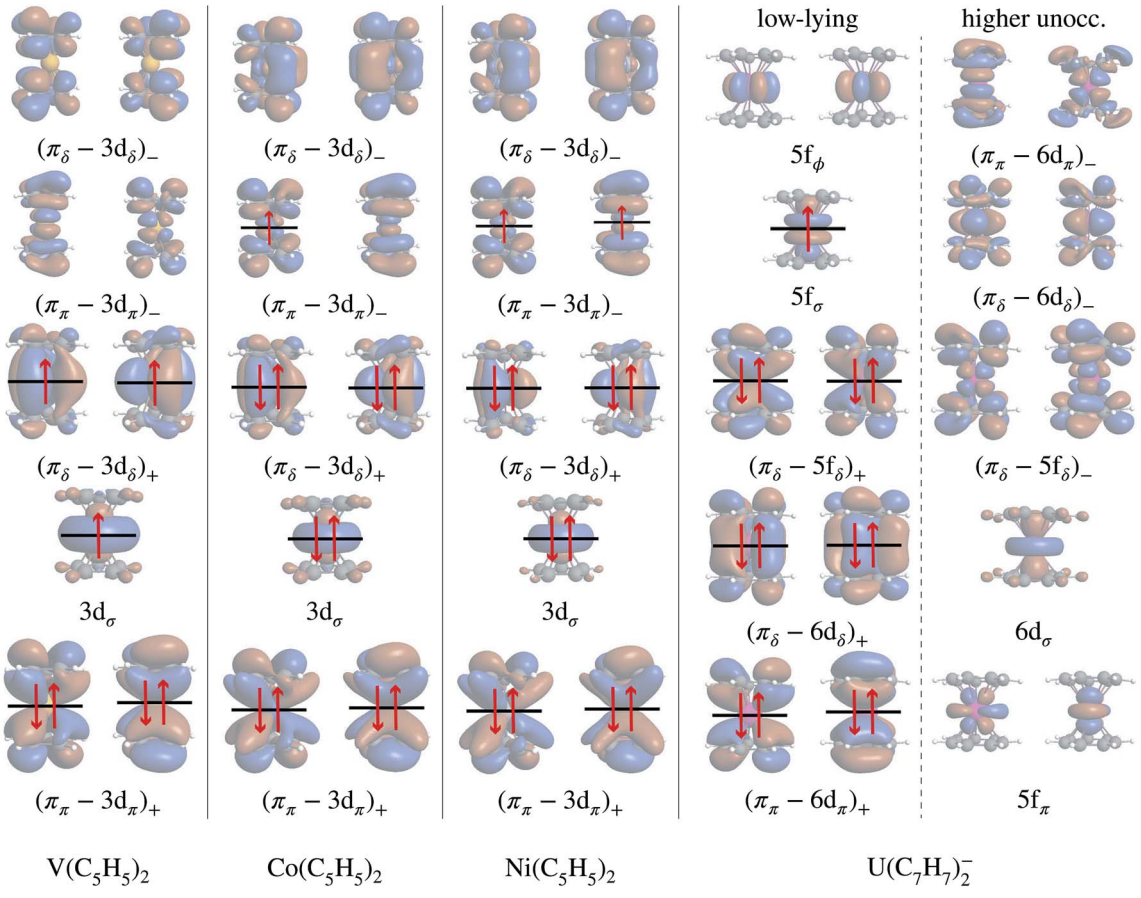

Fig. 2 Frontier MO diagrams for the eclipsed TM metallocenes and $U(C_7H_7)_2^-$, and orbital compositions. The + and − subscripts denote the in-phase bonding and out-of-phase antibonding character. In each column, the energetic ordering is from bottom to top. For cobaltocene, the $D_{5h} \rightarrow C_{2v}$ symmetry reduction lifts the orbital degeneracies without changing the relative ordering of σ, π, and δ, and therefore the diagram is drawn for D_{5h}. The orbitals were obtained from AOC BP/TZ2P DFT calculations in a spin-restricted open-shell fasion and are visualized as isosurfaces (±0.02 a.u.).

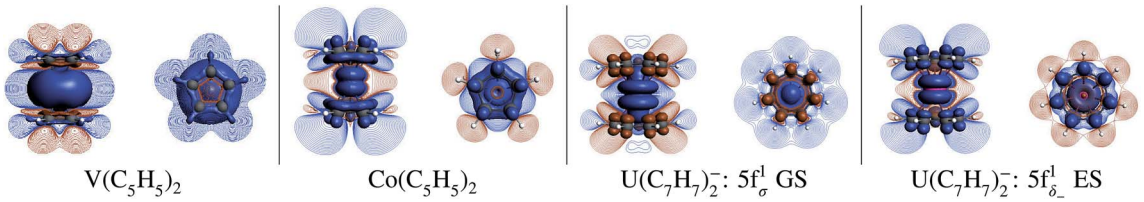

Fig. 3 Spin density distributions (BP/TZ2P, ±0.001 isosurfaces), for the eclipsed TM = V, Co metallocenes and $U(C_7H_7)_2^-$ (experimental geometry for the $5f^1_\sigma$ GS and optimized geometry for the $(\pi_\delta{-}5f_\delta)^1_-$ excited state (ES)), visualized perpendicular (left sub-panels) and parallel to the principal symmetry axis (right). Contour-line plots show the spin polarization in the vertical plane, containing the principal rotational axis, and in the horizontal plane defined by the C atoms of an arene ligand. The spin density plot for nickelocene is very similar to the one of cobaltocene and therefore not shown. Color code: orange (light shading) and blue (dark shading) stand for negative and positive spin density respectively.

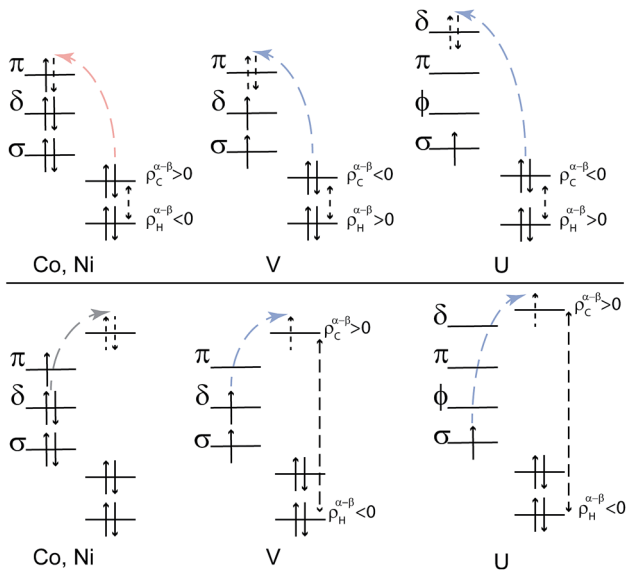

Fig. 4 Simplified schemes showing how a spin density in the TM metallocenes and $U(C_7H_7)_2^-$ may arise at the arene C and H centers due to metal–ligand donation bonding and spin polarization effects. Each individual scheme shows the metal orbitals on the left side and the ligand orbitals of appropriate symmetry on the right side. L–M (top) and M–L (bottom) donation is evidenced with a blue arrow if it is selective for the α spin, and a red arrow if it is selective for the β spin. Double headed vertical arrows indicate spin polarization mechanisms.

polarization then generates negative spin density at the ligand protons, *i.e.* opposite in sign to the carbon spin density. Because the ligand spin density is rooted in covalent effects, it can be sensitive to the choice of the functional in DFT calculations ('delocalization error').[51,99] For the following semi-quantitative discussion of the spin densities, the calculations with the BP functional are deemed to be sufficiently accurate.[28,49,50] It is important to distinguish in the discussion between orbitals of different spin, such that, for instance, $3d^\alpha$ refers collectively to the α spin TM 3d orbitals.

Mulliken and natural population analyses (MPA, NPA) were carried out to determine the atomic spin populations, *i.e.* measures of the integrated spin density per atom. The carbon spin populations in cobaltocene and nickelocene are positive, while the hydrogen spin populations are negative (Tables S3 and S4†). Both for $Co(C_5H_5)_2$ and $Ni(C_5H_5)_2$, L–M donation occurs into the metal $3d_\pi$ orbitals. Nickelocene has a filled $3d^\alpha_\pi$ shell, and therefore only β spin L–M donation can take place as shown in Fig. 4 (see Table S6† for numerical values). In $Co(C_5H_5)_2$, the ligand may donate both spins, but it is clear from the calculations that β over α spin L–M donation is strongly favored (0.95 *vs.* 0.58 electrons respectively, Table S5†). Considering the JT structure, this is easily explained by the JT energy splitting of the $3d_\pi$ shell which renders the β spin donation into the empty lower-energy $3d^\beta_\pi$ orbital (the corresponding $3d^\alpha_\pi$ is filled) favorable over the donation of either spin into the higher-energy $3d_\pi$ spin orbitals. However, the calculations showed that even in the D_{5h} structure with degenerate $3d_\pi$ orbitals, β spin donation is favored. That is, L–M donation bonding is strongly β spin preferential both in nickelocene and cobaltocene.

The preferential β-spin L–M donation leaves the arene π_π framework with excess α-spin density, which is the source of the positive spin-density at the C centers in cobaltocene and nickelocene. A McConnell spin polarization mechanism[34] of the C–H bonds then causes negative spin-density at the protons. These findings are in agreement with old derivations,[36,37,93,96] more recent calculations,[42,50,51] and experimental NMR data.[36,100–103]

M–L back-donation bonding involves predominantly the filled $3d_\delta$ metal orbitals. This donation is about twice as pronounced in cobaltocene than in nickelocene (~0.30 *vs.* 0.15 electrons, see the sums of the $3d^\alpha_\delta$ and $3d^\beta_\delta$ populations in Tables S5 and S6†) but only weakly spin-preferential. Hence, no significant excess spin density arises in the arene π_δ networks from $3d_\delta$ M–L back-donation for the two complexes. The Co and Ni $3d_\sigma$ populations are close to 2 (α and β combined, Tables S5 and S6†), due to their nonbonding character, and therefore also no significant source of ligand spin density. Note that the electron-spin flow due to bonding/back-bonding is essentially the same for the five-fold symmetric and the JT distorted cobaltocene structures.

The ligand spin density pattern in vanadocene is opposite to the Co and Ni counterparts, *i.e.* negative at C and positive at H. In 1960, Levy and Orgel[38] proposed a CF mechanism as follows: the non-bonding $3d_\sigma$ and $3d_\delta$ metal orbitals with single α-spin occupations render a ligand π_π electron transfer into the $3d_\pi$ orbitals energetically more favorable if the transferred electron also has α spin, such as to maximize the number of parallel

spins at the metal. This would lead to an excess of β-spin density at the carbons, and by further spin-polarization within the ligand σ system would create α-spin density at the protons. This hypothesis was called into question in follow-up studies by Prins[37] and Rettig and Drago[36] in 1969. In fact, however, according to Fig. 2 there is a LF MO based mechanism that captures the essence of the Levy–Orgel model: the singly occupied $3d_\sigma$ and $3d_\delta$ metal orbitals are able to spin-polarize the bonding $(\pi_\pi\text{–}3d_\pi)_+$ orbitals that result from the L–M donation bonding, such that the α-spin component $(\pi_\pi\text{–}3d_\pi)^\alpha_+$ is more strongly metal-centered whereas the β-spin component $(\pi_\pi\text{–}3d_\pi)^\beta_+$ is more ligand-centered. This would lead to the expected outcome as far as the C and H spin densities are concerned.

The vanadocene ligand atomic spin populations listed in Table S4† are small, because the core- *vs.* valence-shell spin polarization in the ligands, L–M donation bonding, and M–L back-bonding, cause competing effects. Irrespective of the functional used in the DFT calculations, the Mulliken C and H spin populations have the expected sign (C negative, H positive; see also the plot of the spin density distribution in vanadocene shown in Fig. 3), but the natural spin populations show variations. L–M donation occurs preferentially into the V $3d^\alpha_\pi$ orbitals, due to favorable exchange interactions (aligned spins), and less into $3d^\beta_\pi$ orbitals (Table S6† and Fig. 4), leaving excess β spin in the arene π_π networks. This is in essence the Levy–Orgel mechanism, which causes negative C valence spin densities independently from the interaction of the ligand with the V $3d^\alpha_\sigma$ orbital. Weak α-spin M–L back-donation from the V $3d_\delta$ orbitals has the opposite effect on the carbons. The overall carbon spin populations are therefore small and sensitive to the functional used for the calculation. Some covalent interactions of the $3d_\sigma$ spin orbitals with the arene ligands are evident from Table S6,† but they are weaker than the aforementioned L–M donation and M–L back-donation interactions. The source of the negative and positive spin densities around the C and H atoms, respectively, is rooted in a competing combination of the Levy–Orgel mechanism with subsequent C–H spin polarization, and M–L back-donation of α-spin density.

A recent analysis[42] has shown the singly occupied V $3d^\alpha_\sigma$ orbital to be the main source of β-spin density at the arene carbon nuclei. Due to V being near the beginning of the 3d series, this orbital is radially very extended and overlaps with the C 1s orbitals such that α-spin-selective Pauli repulsion triggers an excess of C 1s β-spin density. Plots of the V $3d^\alpha_\sigma$, Co $3d^\alpha_\sigma$ and Ni $3d^\alpha_\sigma$ natural localized MOs in Fig. 5 clearly show the large radial extension for vanadium. The signs of the ligand spin densities at the atomic nuclei are in line with the observed NMR shifts[39,100,103] and reproduced in NMR calculations.[42,50,52] The arene π orbital contributions to the carbon HyFCCs were quite small. This means that the LF analog of the Levy–Orgel mechanism is affecting the carbon valence shells but it does apparently not produce a strong C 1s core spin polarization in itself.

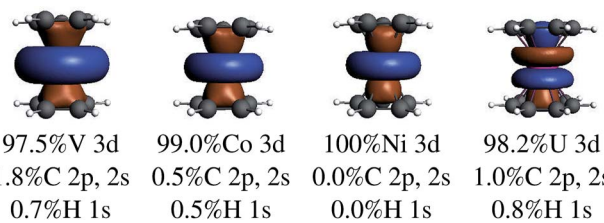

Fig. 5 Metal $3d^\alpha_\sigma/5f^\alpha_\sigma$ natural localized molecular orbital (isosurface value of ±0.02), and its composition, of the different TM metallocenes and $U(C_7H_7)_2^-$. BP/TZ2P calculations. Note the radial contraction of $3d_\sigma$ from V to Co and Ni.

To summarize the interactions in the TM systems: for Co and Ni, the main source of ligand spin density is L–M β-spin donation into the partially filled $3d_\pi$ metal orbitals, leaving excess α spin at the carbons and – *via* spin polarization – excess β spin at the protons. The M–L back donation is not strongly spin selective and weakly reinforces the spin effects from the L–M donation. For V, there is L–M α-spin donation into the empty $3d_\pi$ metal orbitals, leaving excess β spin at the carbons which causes excess α spin at the protons. The M–L back donation from the $3d_\delta$ orbitals in vanadocene is also α spin selective and counter-balances the spin effects of the L–M donation to some extent.

3.2.2 Electronic structure and bonding in $U(C_7H_7)_2^-$. For the $C_7H_7^{3-}$ ligand of $U(C_7H_7)_2^-$ the highest occupied fragment orbital is of π_δ symmetry. L–M donation bonding is therefore facilitated predominantly by the π_δ arene orbitals. The bonding interactions involve both U 5f and 6d orbitals,[28] but we focus here on the 5f orbitals because of the interactions with the unpaired electron in the same shell. Unlike the TM $3d_\pi$ orbitals, the U $5f_\pi$ interact much weaker with the arene π_π MOs, the resulting orbitals being essentially nonbonding. Likewise, the U $5f_\sigma$ orbital is essentially nonbonding, similar to the $3d_\sigma$ orbitals in the TM metallocenes.

In order to rationalize the negative sign of $A^{^1H}_{iso}$ deduced from the magnetic resonance experiments, Gourier *et al.*[27] proposed a scheme for the spin density distribution in $U(C_7H_7)_2^-$ according to which the C and H centers have positive and negative spin densities. The scheme (see Fig. S3†) described a L–M selective β-spin donation mechanism into the singly occupied MO of essentially mixed $5f_\sigma$ (38.5%) and $5f_\pi$ (51.4%) character (dictated by the combined effects of LF and SOC), assuming that the $5f_\sigma$ and $5f_\pi$ orbitals are both covalently bonded. Since the spin density flow according to this scheme is similar to $Co(C_5H_5)_2$, as far as the ligands are concerned, a similar covalent metal–ligand bonding was assumed to be present in the two sandwich complexes.

This conclusion does not hold true according to the present SR-DFT calculations, which consistently predict negative/positive spin densities at the C/H centers (Fig. 3, numerical data in Table S3†). The differences to the mechanism predicted by Gourier *et al.* are related to the non-bonding character of the $5f_\sigma$ orbital which does not promote β-spin donation from the arene π_σ MOs. This is also reflected in Table S5† which shows only a very small occupation of 0.04 of the $5f^\beta_\sigma$ orbital. Likewise, L–M electron donation into the $5f_\pi$ orbitals occurs to only a slight extent, given that the $5f_\pi$ orbitals are also essentially nonbonding, and this donation is not spin selective. Moreover, a similar ligand spin density has been obtained from SR-DFT

test calculations using the experimental distorted geometry for $U(C_7H_7)_2^-$ (not shown).

A comparable bonding scenario between $U(C_7H_7)_2^-$ and $Co(C_5H_5)_2$ as proposed by Gourier *et al.* (Fig. S3†), would be present if the unpaired electron in $U(C_7H_7)_2^-$ would localize in the $(\pi_\delta\text{–}5f_\delta)_-$ MOs. *I.e.* in a CF picture, the U^{V+} ion would have the unpaired electron in the $5f_\delta$ shell. This scenario would indeed be cobaltocene-like: the partially filled U $5f_\delta$ shell would receive preferential β-spin donation from the occupied arene π_δ frontier orbitals, leaving excess α spin at the carbons and spin-polarized proton environments with an excess of β spin.

To confirm this hypothesis, a $(\pi_\delta\text{–}5f_\delta)^1_-$ excited state configuration for $U(C_7H_7)_2^-$ was optimized at the BP/TZ2P level. The obtained geometry was nearly identical to the $(5f_\sigma)^1$ GS, but 1.88 eV (181 kJ mol^{-1}) higher in energy, and the obtained Mulliken (natural) atomic spin populations for the U, C and H centers were 0.663 (0.648), 0.025 (0.026) and −0.001 (−0.001) respectively, *i.e.* close to those obtained for cobaltocene (Table S3†). The striking similarity with the GS of $Co(C_5H_5)_2$ is also clearly seen in the spin density plots in Fig. 3. What renders the bonding scenarios similar now, between the 3d metallocene and the actinocene, is that in each case the highest occupied arene orbitals interact strongly with a partially filled metal valence shell of the same symmetry with respect to the rotational axis, leading to similar donation bonding and – importantly – to very similar spin preferences in this donation bonding. The fact that the donating orbitals are of δ symmetry with respect to the symmetry axis in the actinide case, but of π symmetry in cobaltocene, is secondary. However, this similar bonding and spin-density distribution in the $5f^1$ $U(C_7H_7)_2^-$ and d^7 cobaltocene occurs only if one considers an excited state of the former system that is not populated at room temperature or below.

There are potentially two vanadocene-like mechanisms according to which spin density could be distributed in $U(C_7H_7)_2^-$ GS as a consequence of metal–ligand bonding: a L–M spin-selective donation mechanism (as shown in Fig. 4) and a direct spin-polarization of the ligand σ orbitals. A spin polarization mechanism mediated by the U 6s and 6p orbitals was speculated to operate in the $5f^2$ uranocene complex, $U(C_8H_8)$, driving the ligand ^1H and ^{13}C contact shifts.[104,105] However, as detailed in Section S5,† we found no evidence of a mechanism involving U 6s/p, or a direct polarization as in vanadocene, and overall qualitatively similar spin density distributions and L–M donation mechanisms in the two actinocenes. We leave a discussion of the $U(C_8H_8)$ NMR shifts for a separate study.

Considering a vanadocene-like L–M spin-selective donation bonding (as shown in Fig. 4), this scenario is supported by the fact that the relevant orbitals participate strongly in covalent bonding (Fig. 2). As in vanadocene, selective α-spin donation, favored by exchange interactions in an Orgel–Levy type fashion, occurs into the U $5f_\delta^\alpha$ spin-orbitals, leaving excess β-spin density in the arene π_δ networks which cause the calculated negative C spin populations and ultimately positive H spin populations (Table S3†).

The effect of SOC on the spin density distribution in $U(C_7H_7)_2^-$ will complicate the effects further. As shown in the following section, SOC mixes the $(5f_\sigma)^1$ (∼70%) and the $(5f_\pi)^1$ (∼30%) configurations in the GS of $U(C_7H_7)_2^-$. The mixing is such that $5f_\pi^\beta$ spin-orbitals are populated at the expense of the $5f_\sigma^\alpha$ spin-orbitals, because the SOC mixes opposite spin projections. A L–M donation bonding into the $5f_\delta$ empty orbitals in a $(5f_\pi^\beta)^1$ configuration of the metal would follow a vanadocene-like Orgel–Levy mechanism, too, in the sense that it would be spin-selective such as to maximize the parallel spins at the metal. This aspect is evident from the spin density visualized in Fig. 6 for an excited $(5f_\pi^\beta)^1$ configuration of $U(C_7H_7)_2^-$. The L–M donation is β spin selective and leaves excess α spin density at the carbons. A competing α- *vs.* β-spin L–M donation triggered by the SOC must therefore be expected. However, given that the $(5f_\pi)^1$ configuration has only a minor contribution to the SOC GS of $U(C_7H_7)_2^-$, SOC does not change the signs of the ligand atomic spin populations relative to the SR calculations, it only reduces their magnitudes.

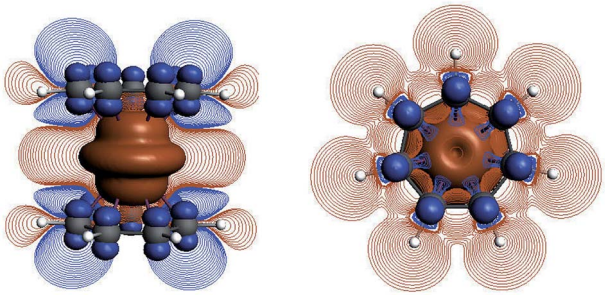

Fig. 6 Spin density distributions (isosurfaces, ±0.001) for the $(5f_\pi^\beta)^1$ excited electronic state of $U(C_7H_7)_2^-$. Contour-line plots show the spin polarization in the vertical plane, containing the seven-fold rotational axis, and in the horizontal plane defined by the C atoms of an arene ligand. AOC BP/TZ2P calculations with optimized structure. Color code: orange (light shading) and blue (dark shading) stand for negative and positive spin density, respectively.

We conclude that a similar metal–ligand bonding takes place in the $5f^1$ $U(C_7H_7)_2^-$ and the $3d^3$ vanadocene. The L–M selective α-spin donation, common to both systems, can be viewed as resulting from interactions by which the number of unpaired spins in formally non-bonding orbitals at the metal is maximized. Since we are concerned with exact or near spatial degeneracies, however, and since the SOC may take a strong influence on the electronic structure of the $5f^1$ $U(C_7H_7)_2^-$, it is important to corroborate the DFT analysis with the help of multi-configurational wavefunction calculations, and with explicit calculations of the magnetic properties. The application of multiconfigurational wavefunction methods to study energetics and bonding scenarios in metallocenes, lanthanocenes and actinocenes has proved to be very valuable previously.[106–111]

3.3 Electronic structure and metal–ligand bonding from wave-function approaches

3.3.1 Electronic structures and bonding in the metallocenes. Fig. 7 displays selected optimized active-space natural orbitals (NOs) and their occupations for the TM metallocenes. Tables S7 and S8† gather the relative energies of low-energy electronic configurations. The CASSCF ('CAS') and CASPT2

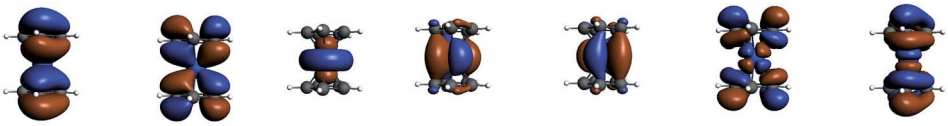

	$(\pi_\pi - 3d_\pi)_+$	$(\pi_\pi - 3d_\pi)_+$	$3d_\sigma$	$(\pi_\delta - 3d_\delta)_+$	$(\pi_\delta - 3d_\delta)_+$	$(\pi_\pi - 3d_\pi)_-$	$(\pi_\pi - 3d_\pi)_-$
$V(C_5H_5)_2$	1.99	1.99	1.00	0.99	0.99	0.02	0.02
$Co(C_5H_5)_2$	1.98	1.92	1.97	1.95	1.95	1.02	0.11
$Ni(C_5H_5)_2$	1.98	1.98	1.98	1.97	1.97	1.02	1.02

Fig. 7 Selected GS NOs and their occupations obtained from CAS-SR calculations on the eclipsed BP/TZ2P geometries of the TM metallocenes. The converged NOs for cobaltocene are shown as isosurfaces (±0.02) and representative of the series.

('PT2') approaches predict GSs that are energetically well separated from the first excited states (ESs) of the same spin multiplicity, for all metallocenes. The ES corresponds essentially to mixed $3d_\sigma/(\pi_\delta{-}3d_\delta)_+ \rightarrow (\pi_\pi{-}3d_\pi)_-$ excitations, *i.e.* formally these are d-to-d ligand-field transitions. As expected, SOC has no qualitative impact on the electronic structures of the TM metallocenes, as it has nearly no effect in the free ions themselves (see Table S9†). Upon a closer look, of course, SOC induces slight zero field splittings (ZFS) in the GSs of vanadocene and nickelocene of ~2 cm^{-1} and ~39 cm^{-1} (PT2-SO), respectively, in good agreement with experimental ZFS parameters D of ~2.8 cm^{-1} for vanadocene[39,91] and ~34 cm^{-1} for nickelocene.[40,112,113]

The various CAS calculations predict an essentially single-configurational GS for each metallocene, as the orbital degeneracy of cobaltocene is split by ~0.42 eV upon the JT distortion (which is roughly the same as the corresponding orbital energy splitting for the α-spin orbitals in the BP DFT calculation). The NOs and their occupations are in qualitative agreement with the DFT calculations, showing that the unpaired electron(s) are localized in the $(\pi_\pi{-}3d_\pi)_-$ MOs in cobaltocene and nickelocene, and in the $3d_\sigma$ and $(\pi_\delta{-}3d_\delta)_+$ MOs in vanadocene. Electron correlation involving the $(\pi_\pi{-}3d_\pi)_+$ and $(\pi_\pi{-}3d_\pi)_-$ MO pairs causes some modest multi-reference character with partial $(\pi_\pi{-}3d_\pi)_-$ occupations, which appears to be the strongest in the GS of cobaltocene, and this correlation is required to obtain the correct ground spin state for this system (see Section S3†). The DFT analysis already revealed that these two pairs of MOs are vital to capture the majority of spin delocalization due to L–M donation bonding in either of the metallocenes. This spin-preferred donation is further confirmed by the CAS-SR GS atomic spin-populations (MPA) collected in Table 1 for $Co(C_5H_5)_2$ and $V(C_5H_5)_2$. However, the signs of the H spin populations in cobaltocene, and of C in vanadocene are not reproduced by CAS-SR calculations with attainable active spaces, because they are dominated by spin polarization of the arene σ networks. An even qualitative description of these effects requires much larger active spaces, for which an orbital optimization becomes impractical. The signs for the C and H atomic spin-populations in cobaltocene and vanadocene in Table 1 agree qualitatively with those from the DFT calculations when a much larger orbital active space is used in a 'RASCI' approach (see details in Section S2†).

3.3.2 Electronic structure and bonding in $U(C_7H_7)_2^-$. Characterizations of the low-energy electronic states of $U(C_7H_7)_2^-$ are provided in Table 2. The NOs and their occupations are shown in Fig. 8. The interested reader is directed to Tables S10–S12† for results obtained with different active spaces, equilibrium geometries, and basis sets.

Without SOC, the GS is $^2\Sigma$ and the wavefunction is mostly single-configurational. The dominant configuration is $(5f_\sigma)^1$ with about 80% weight. The next most important weight corresponds to excited configurations in which electrons are promoted from $(\pi_\delta{-}5f_\delta)_+$ to $(\pi_\delta{-}5f_\delta)_-$ MOs, as indicated by the GS NO occupations listed in Table 2 and Fig. 8. Above $^2\Sigma$ appear two orbitally doubly degenerate states, first $^2\Phi$ and then $^2\Pi$. Similar to the GS, these states are dominated by the expected $(5f_\phi)^1$ and $(5f_\pi)^1$ configurations, and the wavefunctions have contributions from configurations that correspond to $(\pi_\delta{-}5f_\delta)_+$ to $(\pi_\delta{-}5f_\delta)_-$ excitations. That is, these low-energy states are mainly assigned to single-electron LF transitions among the U $5f_\sigma$, $5f_\pi$, and $5f_\phi$ orbitals, while the electron correlation mixes $(\pi_\delta{-}5f_\delta)_+$ to $(\pi_\delta{-}5f_\delta)_-$ excited configurations into the respective wavefunctions. At a much higher energy, ~1.9 eV with CAS-SR and ~1.8 eV with PT2-SR, occurs the $^2\Delta$ state where the unpaired electron populates the antibonding $(\pi_\delta{-}5f_\delta)_-$ MOs, in agreement with DFT/BP results (see the previous section and ref. 28).

Table 1 GS atomic spin populations obtained from *ab initio* wavefunction calculations[ab]

System/approach	Metal center	C	H
$Co(C_5H_5)_2$	Co	C	H
CAS(11, 12)-SR	0.830	0.015	*0.002*
RASCI[c]	0.820	0.020	−0.002
$V(C_5H_5)_2$	V	C	H
CAS(7, 7)-SR	*2.960*	*0.003*	*0.001*
RASCI[c]	3.030	−0.004	0.001
$U(C_7H_7)_2^-$	U	C	H
CAS(9, 13)-SR	1.218	−0.015	*−0.001*
RASCI[c]	1.216	−0.014	*−0.001*

[a] The eclipsed BP/TZ2P geometries are used for the TM metallocenes and the eclipsed experimental geometry is used for the actiocene. [b] Italic type is used to indicate that the dimension of the configuration interaction space is too small to create qualitatively correct spin populations. [c] See Section S2 for details on the chosen RAS subspaces.

Table 2 Low-lying electronic states for $U(C_7H_7)_2^-$: wavefunction compositions and relative energies obtained from CAS-SR/SO (PT2-SR/SO data in parentheses)[a]

State	Composition[b]	ΔE (eV)	Composition[c]	ΔE (eV)
CAS(9, 13)-SR			CAS(9, 13)-SO	
$^2\Sigma$	$(6d_\delta^+)^{3.95}(5f_\delta^+)^{3.74}(5f_\sigma)^{0.99}(5f_\delta^-)^{0.24}$	0.00 (0.00)	$70\%^2\Sigma + 30\%^2\Pi$	0.00 (0.00)
$^2\Phi$	$(6d_\delta^+)^{3.94}(5f_\delta^+)^{3.74}(5f_\phi)^{0.99}(5f_\delta^-)^{0.25}$	0.29 (0.40)	$98\%^2\Phi + 2\%^2\Delta$	0.17 (0.28)
$^2\Pi$	$(6d_\delta^+)^{3.95}(5f_\delta^+)^{3.72}(5f_\pi)^{0.99}(5f_\delta^-)^{0.23}$	0.50 (0.47)	$92\%^2\Pi + 8\%^2\Delta$	0.82 (0.80)
$^2\Delta$	$(6d_\delta^+)^{3.94}(5f_\delta^+)^{3.56}(5f_\delta^-)^{0.97}(5f_\phi)^{0.23}(5f_\pi)^{0.15}$	1.91 (1.83)	$70\%^2\Pi + 30\%^2\Sigma$	0.93 (0.92)
			$100\%^2\Phi$	0.94 (1.06)
			$92\%^2\Delta + 8\%^2\Pi$	2.13 (2.07)
			$98\%^2\Delta + 2\%^2\Phi$	2.39 (2.32)

[a] The eclipsed experimental geometry is used. [b] The compositions of the SR wave functions are given in terms of the NOs that are significantly populated; the $6d_\delta^+$, $5f_\delta^+$ and $5f_\delta^-$ notations are used for brevity instead of $(\pi_\delta–6d_\delta)_+$, $(\pi_\delta–5f_\delta)_+$ and $(\pi_\delta–5f_\delta)_-$ (see Fig. 8). [c] Given in terms of the SR states on the first column.

The electronic structure of $U(C_7H_7)_2^-$ is dictated by a delicate interplay between SOC and LF effects. If one considers a free U^V ion, the SOC splits (Table S9†) the ^2F SR ground term into the sixfold degenerate $^2F_{5/2}$ and eightfold degenerate $^2F_{7/2}$ SOC levels, characterized by a total angular momentum $J = 5/2$ and 7/2, and the projections $M_J = J, \ldots, -J$. In the complex, (i) each J manifold splits into Kramers doublets, and (ii) due to the high symmetry, M_J remains a good quantum number such that states of different J but same M_J mix. For example, $|J, M_J\rangle = \left|\frac{5}{2}, \pm\frac{1}{2}\right\rangle$ and $\left|\frac{7}{2}, \pm\frac{1}{2}\right\rangle$ free ion spinors may mix, which serves to adjust the relative admixture of the SR $^2\Sigma$ and $^2\Pi$ components of opposite spin in the SOC GS. The SOC can also mix $^2\Pi$ with $^2\Delta$, and $^2\Delta$ with $^2\Phi$. Since the $^2\Delta$ state is high in energy, its SOC mixing with the other states is insignificant (Table 2), which also causes the $^2\Phi$ states to undergo only weak SOC. Pronounced SOC mixing occurs between the closely spaced $^2\Sigma$ and $^2\Pi$ states.

The SOC GS is clearly of $^2\Sigma$ parentage (70%) but exhibits a sizable $^2\Pi$ weight (30%) as shown in Table 2. The $^2\Sigma$–$^2\Pi$ SOC mixing is also evident through the comparison of the natural occupations listed in Fig. 8, which shows that under the effect of SOC, ~0.3 electrons are depleted from the $5f_\sigma$ orbital and redistributed among the $5f_\pi$ orbitals. The CAS(9, 13)-SR(SO) and PT2(9, 13)-SR(SO) potential surface scans (Fig. S2†) along the metal-ring distances show, however, that the structures obtained with or without the treatment of SOC are identical, due to the predominantly non-bonding nature of the $5f_\sigma$ and $5f_\pi$ orbitals. This is also the reason why the SR-DFT structure

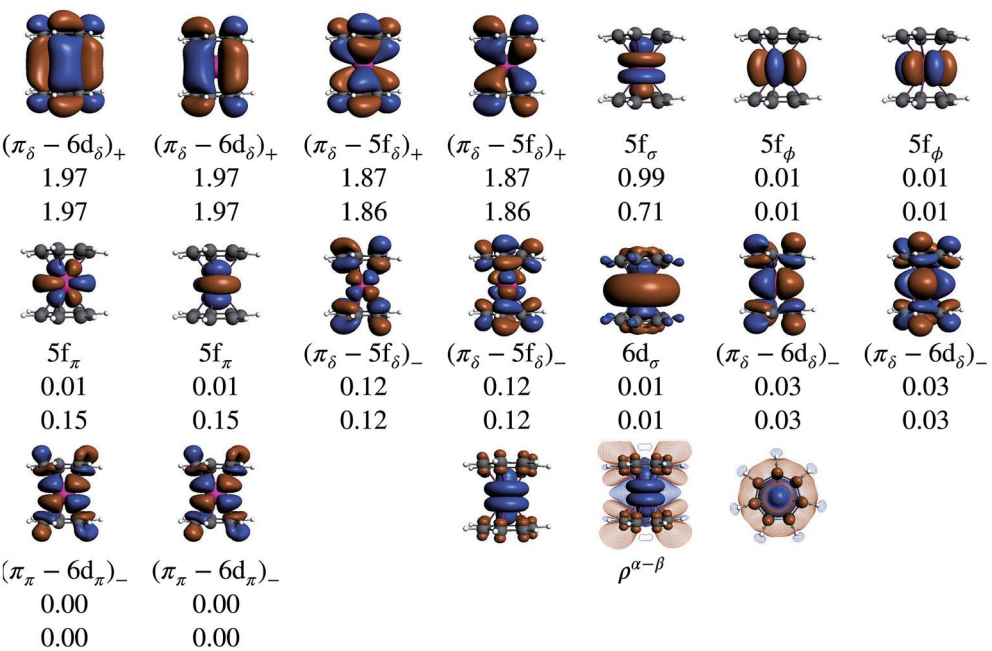

Fig. 8 NOs (isosurface value of ±0.02) and their occupations for the $U(C_7H_7)_2^-$ GS, obtained through CAS(9, 13) calculations on the eclipsed experimental structure. SR and SOC occupations are listed on the first and second line respectively. The GS CAS(9, 13)-SR spin density ($\rho^{\alpha-\beta}$) is also visualized with an isosurface of ±0.001. Color code for $\rho^{\alpha-\beta}$: orange (light shading) and blue (dark shading) stand for negative and positive spin density, respectively.

optimizations are reliable. The obtained PT2-SO and the experimental metal-aryl distances (1.98 Å) are identical, proving the adequacy of the active space in capturing the bonding interactions in this actinocene.

It is worth noting that Gourier *et al.*[27] assigned a dominant $5f_\pi^1$ character, instead of $5f_\sigma^1$, for the GS of $U(C_7H_7)_2^-$, based on a CF analysis of the *g* factors. Gourier *et al.* established that the $\left|\frac{5}{2}, \pm\frac{1}{2}\right\rangle$ Kramers pair dominates the SOC GS. The electron density weight for these spinors is 57.1% $5f_\pi$ and 42.9% $5f_\sigma$.[114] To achieve agreement of the calculated and the measured *g* factors, however, a mixing of the $\left|\frac{5}{2}, \pm\frac{1}{2}\right\rangle$ with $\left|\frac{5}{2}, \pm\frac{5}{2}\right\rangle$ spinors was proposed (in proportions of about 90% and 10%), which would only be allowed if the high symmetry of the complex were removed. The composition of the $\left|\frac{5}{2}, \pm\frac{5}{2}\right\rangle$ spinors is $5f_\delta$ (14.2%) and $5f_\phi$ (85.8%),[27,114] such that the mixing would introduce $5f_\delta$ and $5f_\phi$ character in the GS. The final SOC GS composition was concluded to be $5f_\pi$ (51.4%), $5f_\sigma$ (38.5%), $5f_\phi$ (8.9%) and $5f_\delta$ (1.5%). A derivation is presented in Section S4.† The difference with the GS composition predicted by the *ab initio* calculations arises from the fact that in the LF picture the $5f_\pi$ metal orbitals are destabilized relative to $5f_\sigma$, which reduces the π contributions in the GS relative to the $\left|\frac{5}{2}, \pm\frac{1}{2}\right\rangle$ free-ion spinors. This mechanism involves free-ion states of different *J* but same M_J that are allowed to mix under the linear symmetry of the complex, but not in the free metal ion.

Table 1 lists GS atomic spin populations obtained from CAS(9, 13)-SR and RASCI approaches. An isosurface plot of the CAS(9, 13)-SR spin density is shown in Fig. 8. In agreement with DFT (Table S3†), the wavefunction calculations predict negative spin populations at the carbons, and an excess of α spin density at uranium beyond the formal single occupation. As already stated in the DFT analysis, positive spin populations at the H centers are then caused by the McConnell polarization mechanism, which acts *via* the ligand σ networks. Attempts to capture this polarization *via* RASCI calculations were unsuccessful due to technical limitations regarding the size of the active space. Nonetheless, the wavefunction calculations show clearly that, in the GS of $U(C_7H_7)_2^-$, an electron flow within the π system, facilitated in particular by the metal–ligand bonding $(\pi_\delta\text{–}5f_\delta)_+$ MOs, creates negative spin density at the ligand C centers, in agreement with the DFT calculations. Agreement was further noted for the spin populations of the U and C atoms in the $^2\Pi$ and $^2\Delta$ excited states. For instance, in the $^2\Delta$ excited state, values of 0.675 and 0.021, respectively, were obtained, which are similar to those obtained from BP/TZ2P. Therefore, the *ab initio* wavefunction calculations confirm that a cobaltocene-like spin density distribution in $U(C_7H_7)_2^-$, *i.e.* with excess α spin density at the carbons due to L–M β-spin donation into a partially filled metal shell, occurs only in a high-energy excited state.

In order to visualize the effect of SOC on the spin magnetization ('spin density') in $U(C_7H_7)_2^-$, isosurfaces of the GS natural spin-orbitals (NSOs)[108,114,115] and spin magnetizations are shown in Fig. 9. CAS-SO spin and angular momentum expectation values, $\langle S\rangle$ and $\langle L\rangle$, are listed in Table S13.† The ∥ direction is along the principal axis of symmetry, coinciding with the *z* direction. Without SOC and with the usual choice of *z* for the spin quantization axis, the spin magnetization corresponds to the usual spin density, and $\langle S_\parallel\rangle$ would be equal to M_S. The $\langle S_\parallel\rangle$ and $\langle L_\parallel\rangle$ are around ±0.197 and ±0.298, *i.e.* very different from the $\langle S_\parallel\rangle = \pm 0.5$ for a SR spin-doublet GS and $\langle L_\parallel\rangle = 0$ for an unpaired electron in the $5f_\sigma$ orbital. The NSO data reaffirm that the difference in the SOC and SR $\langle S_\parallel\rangle$ and $\langle L_\parallel\rangle$ values is caused predominantly by the SOC mixing of the $5f_\sigma$ and $5f_\pi$ orbitals, and, to a lesser extent, by the $5f_\delta$ admixture in the SR wavefunction (Fig. 9). The ∥ spin magnetization ($m_\parallel$) is concentrated in a prolate shape around the actinide center, clearly showing its origin from the spins at the uranium center. The spin magnetization plots also show important contributions from the ligand π network, facilitated by the covalent π_δ–$5f_\delta$ interactions. Indeed, the $5f_\delta$ and $6d_\delta$ bonding NSOs bring positive contributions to the metal-based spin magnetization, meanwhile the corresponding antibonding NSOs bring negative contributions to the largely ligand-based spin magnetization which is ultimately seen in either plot of $m_\parallel$. The behavior appears similar to the LF Levy–Orgel mechanism for the spin density distribution in vanadocene.

3.4 Magnetic properties

3.4.1 *g* factors. The calculated *g* factors for the TM metallocenes (Table 3 for TM = Co and Table S14† for TM = V, Ni) agree well with the experimental data, irrespective of the used computational approach. Notably, axial *g* tensors are obtained for $V(C_5H_5)_2$ and $Ni(C_5H_5)_2$ with *g* factors close to $g_e = 2.0023$. For cobaltocene, the *g* tensor is rhombic. For this system, various experiments delivered a range of different values for the three *g* components, all significantly below g_e. The experimental data collected in Table 3 were derived from EPR by Rudin *et al.* for cobaltocene diluted in a $Mn(C_5H_5)(CO)_3$ host crystal.[41] A more extensive EPR study was performed by Hulliger *et al.* who found the three rhombic *g* factors to be 1.16, 1.38 and 1.94 in a nickelocene host, 1.14, 1.22 and 1.59 in a ruthenocene host, and 1.69, 1.81 and ~1.81 in a ferrocene host.[116]

For $U(C_7H_7)_2^-$, the only experimental data available are from the EPR study of Gourier *et al.*[27] who reported an axial *g* tensor with $\pm g_\parallel = 1.24$ and $\pm g_\perp = 2.37$. The *g* factors predicted by CAS(PT2)-SO calculations are in good agreement with the measurements (Table 3). A comparison between the *g* factors obtained with the different active spaces (see Table S15†) reveals the origins of the $g_\parallel$ and $g_\perp$ components. $g_\parallel$ is predicted roughly similar by all of the active spaces and therefore it is due to the SOC of the $5f_\sigma$ and $5f_\pi$ orbitals in the presence of the ligands, creating an orbital magnetic moment. On the other hand, the magnitude of $g_\perp$ is driven by the metal–ligand bonding and dictated by the $5f_\delta$ admixture into the GS. The differences from $|g_\parallel| = 0.86$ and $|g_\perp = 2.57|$ for idealized $\left|\frac{5}{2}, \pm\frac{1}{2}\right\rangle$ spinors shows how the measured and calculated *ab initio* *g*-factors indicate the deviations of the GS wavefunction from the free-ion Kramers pair. It is important to reiterate that the observed $|g_\parallel| = 1.24$ is closely tied to a much larger contribution of $5f_\sigma$ in the GS than it

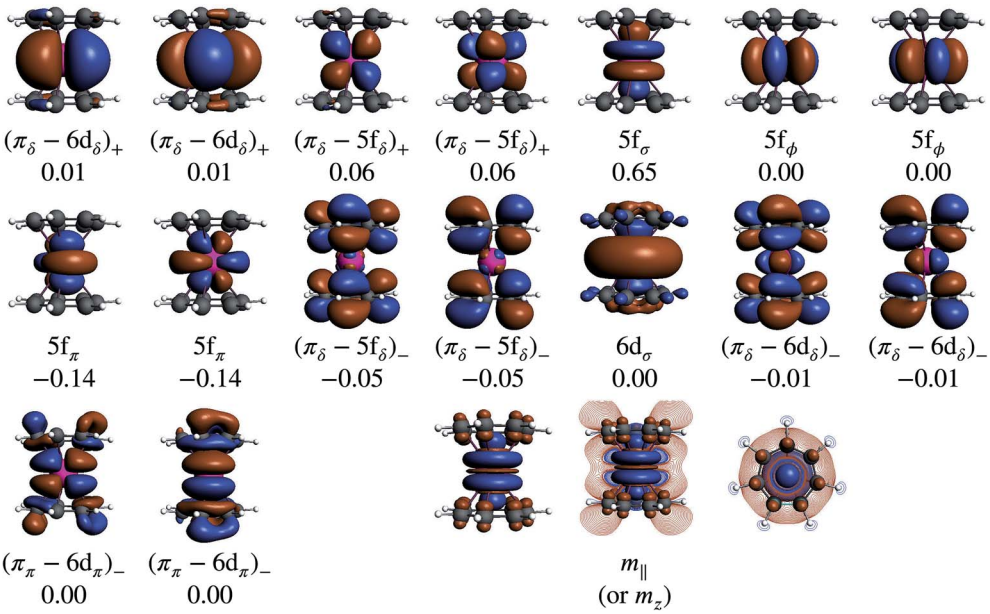

Fig. 9 NSOs and spin populations for a magnetic field along the ∥ direction (along the principal symmetry axis), for the $U(C_7H_7)_2^-$ GS component with $\langle S_Z \rangle > 0$, from CAS(9, 13)-SO calculations. The spin-magnetization component $m_\parallel$ is also shown. The spin populations add up to 2 $\langle S_\parallel \rangle$. Isosurface values: ±0.02 (NSOs), ±0.001 (spin magnetization). For $m_\parallel$, the polarized magnetization in the vertical plane containing the seven-fold rotational axis and in the horizontal plane defined by the C atoms of an arene ligand, are also shown. Color code for $m_\parallel$: orange (light shading) and blue (dark shading) correspond to negative and positive contributions.

is present in the free ion spinors. This also implies that, in the GS of $U(C_7H_7)_2^-$, there is actually a LF admixture of the $\left|\frac{5}{2}, \pm\frac{1}{2}\right\rangle$ and $\left|\frac{7}{2}, \pm\frac{1}{2}\right\rangle$ free ion spinors.

The g factors predicted by relativistic DFT calculations expose some difficulties to capture the delicate balance between LF and SOC in the $U(C_7H_7)_2^-$ GS with this single-configuration approach. The SR-ZORA calculations with a pure functional, treating SOC as a linear perturbation, give $g_\parallel$ close to g_e and a nearly vanishing $g_\perp$. This is due to the failure of perturbation theory to recover the strong effect of SOC on $g_\parallel$, and due to the inability to account for the multiconfigurational GS, which affects $g_\perp$. It is worth noting that the SR-ZORA approach yields correct g factors for the TM metallocenes since these systems are neither governed by strong SOC nor do they have multiconfigurational GSs. When SOC is introduced self-consistently in the SO-ZORA DFT calculations, and notably when a hybrid functional is used, the $U(C_7H_7)_2^-$ $g_\parallel$ greatly improves but $g_\perp$ does not. That is, the strong SOC is accounted for correctly, but the multiconfigurational GS is still not described well. g factors for various excited states of $U(C_7H_7)_2^-$ were calculated using the SO-ZORA/BP approach, and compared to PT2(9, 13)-SO (Table 4). The DFT and wavefunction calculations give comparable relative energies between the different states, and the excited state g factors agree very well, too. The excited states are orbitally degenerate, but otherwise they have less of a multiconfigurational character than the GS. Consequently, the state energies and g factors are well described by SO-ZORA DFT calculations where each degenerate pair of orbitals shares the electron occupation evenly.

Table 3 Calculated GS g factors for cobaltocene and $U(C_7H_7)_2^-$ [a]

		$Co(C_5H_5)_2$			$U(C_7H_7)_2^-$	
	Approach	g_1	g_2	g_3	$g_\parallel$	$g_\perp$
BP	SR-ZORA[b]	1.84	2.01	2.05	2.00	0.43
	SO-ZORA	1.84	2.01	2.05	1.42	1.15
PBE	SR-ZORA[b]	1.83	2.01	2.05	2.00	0.42
	SO-ZORA	1.83	2.00	2.05	1.43	1.10
B3LYP	SO-ZORA	1.47	1.52	2.47	1.37	1.28
PBE0	SO-ZORA	1.51	1.51	2.46	1.34	1.34
CAS-SO[c]		1.78	2.04	2.16	1.38	2.27
PT2-SO[c]		1.77	2.03	2.16	1.36	2.33
Expt.[d]		1.73	1.89	1.96	1.24	2.37

[a] The JT geometry is used for cobaltocene and the eclipsed experimental geometry is used for $U(C_7H_7)_2^-$. [b] Perturbative treatment of SOC. [c] The CAS(11, 12) is used for cobaltocene and the CAS(9, 13), for $U(C_7H_7)_2^-$. [d] Data from ref. 41 for cobaltocene and from ref. 27 for $U(C_7H_7)_2^-$.

3.4.2 Isotropic ^{1}H and ^{13}C HyFCCs. Sizable isotropic ligand HyFCCs are usually associated with the Fermi-contact electron spin mechanism and formally relate to the presence of spin density at the probed nuclei due to covalent bonding between a paramagnetic center and the ligands, and spin polarization. In this case, the isotropic HyFCC for a given C or H atom in the ligands is proportional to the spin magnetization (spin density) at the nucleus and has the same sign as the latter. Due to practical limitations of the CAS approach to produce an accurate atomic core spin polarizations within the ligands, we resorted to a variety of DFT methods for the HyFCC calculations. Isotropic ^{13}C and ^{1}H HyFCCs are listed in Table 5 for cobaltocene and $U(C_7H_7)_2^-$, and in Table S16† for vanadocene and nickelocene. For the JT structure of cobaltocene, the $A_{iso}^{^{13}C}$

Table 4 Calculated g factors for various SOC states of $U(C_7H_7)_2^{-}$[a]

	SO-ZORA/BP			PT2(9, 13)-SO		
SO state	ΔE^b (eV)	$g_\parallel$	$g_\perp$	ΔE^b (eV)	$g_\parallel$	$g_\perp$
$^2\Sigma_{1/2}$	0.00	1.42	1.15	0.00	1.36	2.33
$^2\Phi_{5/2}$	0.31	3.96	0.00	0.27	4.08	0.00
$^2\Pi_{3/2}$	0.75	3.67	0.00	0.80	3.78	0.02
$^2\Delta_{5/2}$	2.35	5.93	0.00	2.32	5.70	0.01

[a] The eclipsed experimental geometry is used. [b] The SO-ZORA relative energies are obtained in ΔSCF calculations while the PT2-SO excitation energies are from Table 2.

and $A_{iso}^{^1H}$ correspond to the average of the individual isotropic HyFCCs.

For the metallocenes, the calculated $A_{iso}^{^{13}C}$ and $A_{iso}^{^1H}$ vary among different functionals but are in qualitative agreement and in reasonable quantitative agreement with available measurements. As in the case of the g factors, the weak SOC is sufficiently accounted for by the SR-ZORA plus perturbative SOC approach. The signs of $A_{iso}^{^{13}C}$ and $A_{iso}^{^1H}$ in the different metallocenes are in agreement with the signs of the calculated atomic spin populations and further validate the deduced mechanisms that cause the spin density distributions due to metal–ligand bonding. In particular, positive and negative $A_{iso}^{^{13}C}$ and $A_{iso}^{^1H}$ are predicted for cobaltocene, in agreement with the positive and negative atomic spin populations that arise through the covalent metal–ligand bonding interactions.

DFT is expected to give reasonable ligand HyFCCs also for $U(C_7H_7)_2^{-}$, since they are not as sensitive to the mixing among the different non-bonding uranium orbitals as the g-tensor. At the SR level, irrespective of the used functional, the $A_{iso}^{^{13}C}$ and $A_{iso}^{^1H}$ are negative and positive, respectively, in agreement with the signs of the calculated C and H atomic spin populations. The sign of $A_{iso}^{^1H}$ is in disagreement with that of cobaltocene, but also with the measurement. Rather, the calculated SR $A_{iso}^{^1H}$ for $U(C_7H_7)_2^{-}$ is in qualitative agreement with that of vanadocene.

The reader is reminded that the spin density distribution (and, to some degree, its mechanism), due to metal–ligand bonding, is similar for $U(C_7H_7)_2^{-}$ and vanadocene, but not cobaltocene or nickelocene. The empty $5f_\delta$ orbitals of the U center and the partially filled $3d_\pi$ orbitals of the Co center, that are primarily involved in metal–ligand bonding, are responsible for opposite signs of the carbon spin densities within $U(C_7H_7)_2^{-}$ and cobaltocene, and therefore ultimately also for the sign of the electron spin contributions to $A_{iso}^{^1H}$.

Strikingly, however, when the strong SOC is introduced in the calculations, *via* the SO-ZORA approach, the predicted $A_{iso}^{^1H}$ for $U(C_7H_7)_2^{-}$ changes sign and agrees in sign and order of magnitude with the one predicted for cobaltocene, and with the measured one. The 1.7 to 1.2 MHz deviations between the SO-ZORA DFT data and the experimental value may appear large at first, but we must emphasize that the SOC improves the calculated $A_{iso}^{^1H}$ by more than 6 MHz toward the experiment and restores the correct sign. This finding strongly suggests that the observed negative sign for the proton HyFCC in $U(C_7H_7)_2^{-}$ is governed by strong SOC and the orbital angular momentum that it creates. Consequently, the HyFCC is dominated by the PSO (paramagnetic interaction of the nuclear spin with the electron orbital angular momentum) mechanism, which happens to be opposite to the sign of the spin density at the protons. Note that PSO-type mechanisms were also found to be dominant for pNMR ligand shifts in several actinide systems.[45] As hypothesized in the introduction, the metal–ligand covalent bonding in the ground states of $U(C_7H_7)_2^{-}$ and cobaltocene is very different, as far as the spin density is concerned, while the same sign and order of magnitude for $A_{iso}^{^1H}$ is caused by SOC in $U(C_7H_7)_2^{-}$.

Table 5 Calculated isotropic HyFCCs (MHz) for cobaltocene and $U(C_7H_7)_2^{-}$[a]

		$Co(C_5H_5)_2$		$U(C_7H_7)_2^{-}$	
Functional	Approach	$A_{iso}^{^{13}C}$	$A_{iso}^{^1H}$	$A_{iso}^{^{13}C}$	$A_{iso}^{^1H}$
BP	SR-ZORA	4.95	−2.97	−0.59	5.10
	SR-ZORA[b]	4.85	−2.97	−0.18	5.19
	SO-ZORA	4.81	−2.97	−0.64 (−1.55)[c]	−1.33 (−0.95)[c]
PBE	SR-ZORA	5.39	−2.86	−0.69	5.02
	SR-ZORA[b]	5.28	−2.86	−0.28	5.12
	SO-ZORA	5.37	−2.86	−0.65	−1.34
B3LYP	SR-ZORA	5.56	−1.85	−1.12	4.99
	SO-ZORA	5.43	_1.86	−0.61	−1.15
PBE0	SR-ZORA	6.00	−1.96	−1.36	5.32
	SO-ZORA	5.88	−1.97	−0.64 (−2.20)[c]	−1.15 (−1.48)[c]
Expt.[d]		—	−2.4	—	−2.7

[a] GS data. The JT BP/TZ2P geometry is used for cobaltocene while the eclipsed experimental geometry is used for $U(C_7H_7)_2^{-}$. [b] Perturbative treatment of SOC. [c] The value in parenthesis were obtained from a spin-unrestricted collinear SO-ZORA calculation using TZP basis sets. [d] Data from ref. 41 for cobaltocene and from ref. 27 for $U(C_7H_7)_2^{-}$.

4 Conclusions

The aim of this study was to investigate whether there is a similarity in the metal–ligand (M–L) bonding occuring in actinide and TM complexes. Metallocenes were chosen for this investigation, because a similarity of bonding between the $5f^1$ $U(C_7H_7)_2^{-}$ and $3d^7$ cobaltocene sandwich complexes had been postulated previously, based on experimental magnetic resonance data and a theoretical analysis.[27] The calculated spin density distributions within the two systems are very different, however, with or without a SOC treatment, and consistent between DFT and CAS wavefunction calculations. The differences were tracked-down to different 5f *vs.* 3d covalent bonding scenarios. On the other hand, the $5f^1$ $U(C_7H_7)_2^{-}$ has similar M–L bonding characteristics as the $3d^3$ vanadocene.

Unlike the electronic GSs of the metallocenes, which are well-defined single configurational and hardly influenced by SOC, the GS of $U(C_7H_7)_2^{-}$ is multiconfigurational with important weights on the $5f_{\delta_+}^4 5f_m^1 5f_{\delta_-}^0$ and $5f_{\delta_+}^{4-n} 5f_m^1 5f_{\delta_-}^n$ configurations ($m = \sigma, \pi$; $n = 1, 2$). The $5f_\pi$ and $5f_\delta$ occupations in the GS are due to strong SOC and ligand-to-metal donation bonding, respectively, and they refine the magnitudes of the $g_\parallel$ and $g_\perp$ components of the axial g tensor. DFT, with an appropriate

treatment of relativistic effects, can provide accurately the $g_{\|}$ component, but a multiconfigurational spin–orbit coupled wave function approach is needed to recover an accurate $g_{\perp}$ component as well. The TM metallocene g values are predicted accurately with both DFT and *ab initio* wavefunction approaches.

In cobaltocene and nickelocene, the metal center is involved in strong covalent bonding with filled arene π_{π} MOs, resulting in selective β-spin density ligand-to-metal donation into the partly filled $3d_{\pi}$ metal orbitals. This process leaves excess α spin density at the arene C atoms. A McConnell spin polarization mechanism then causes negative spin density at the arene H atoms. Therefore, negative ^{1}H isotropic HyFCC is predicted, in agreement with measurements.[36,41]

This spin density distribution mechanism is not present in the $5f^{1}$ $U(C_7H_7)_2^{-}$, mainly because the bonding here involves ligand π_{δ} MOs and empty $5f_{\delta}$ orbitals. A selective α-spin density ligand-to-metal donation then leaves negative spin density at the arene C atoms, and a McConnell spin-polarization mechanisms creates positive spin density at the arene H atoms. This mechanism is very similar to how ligand spin density in vanadocene would arise by considering selective α-spin donation from filled ligand π_{π} orbitals into the empty V $3d_{\pi}$ orbitals.

The electron spin contribution to the $U(C_7H_7)_2^{-}$ ^{1}H isotropic HyFCC is opposite to that in cobaltocene, in agreement with the signs of the ligand atomic spin populations, and therefore confirms the established spin density distributions and underlying mechanisms. However, calculations that properly treat the strong SOC predict ^{1}H isotropic HyFCCs that are consistent in sign and order of magnitude with those of cobaltocene, and that agree with the measured data.[27] SOC does not qualitatively affect the ligand spin density in $U(C_7H_7)_2^{-}$. Instead, a large 'PSO' hyperfine coupling contribution arises from the orbital angular momentum created by the SOC.

The similar ^{1}H isotropic HyFCC in the $5f^{1}$ $U(C_7H_7)_2^{-}$ and the $3d^{7}$ cobaltocene is due to the strong SOC in the former, rather than similar metal–ligand bonding. Instead, the $5f^{1}$ $U(C_7H_7)_2^{-}$ and the $3d^{3}$ vanadocene share similar bonding characteristics, in the sense that the highest occupied ligand π orbital has the same nodal structure as a pair of empty metal valence orbitals, causing donation bonding into these metal orbitals, donation which, due to unpaired spins in other non-bonding metal orbitals, is rendered selective for the α spin. A concluding scheme for $U(C_7H_7)_2^{-}$ is shown in Fig. 10.

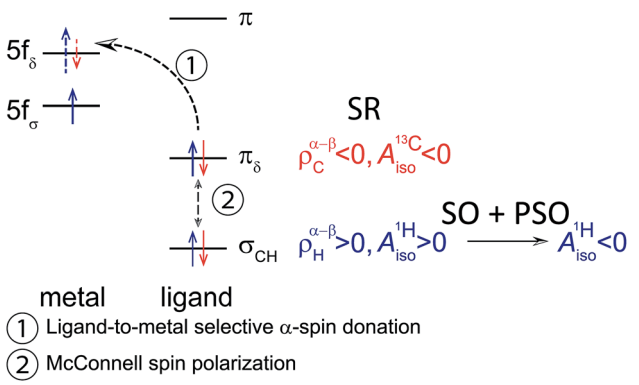

Fig. 10 Simplified scheme concluding the underlying mechanism for the spin density (ρ) (spin magnetization (m)) distribution in $U(C_7H_7)_2^{-}$ which drives the signs of the arene ^{13}C and ^{1}H isotropic HyFCCs.

Through the use of relativistic quantum chemical methods and bonding analysis tools, the present study offers insight into the similarities and differences of ligand to metal donation bonding, and the resulting spin density distributions in the ligands, for transition metals *vs.* actinides. For the systems studied herein, the analysis shows that experimental HyFCCs (and, by extension, paramagnetic NMR shifts) can be very powerful indicators of the donation bonding, but SOC can very much complicate the picture.

Conflicts of interest

There are no conflicts to declare.

Acknowledgements

The authors acknowledge support from the U.S. Department of Energy, Office of Basic Energy Sciences, Heavy Element Chemistry program, under grant DE-SC0001136 (formerly DE-FG02-09ER16066). We thank the Center for Computational Research (CCR) at the University at Buffalo for providing computational resources.

References

1 A. Haaland, *Acc. Chem. Res.*, 1979, **12**, 415–422.
2 B. E. Bursten and R. J. Strittmatter, *Angew. Chem., Int. Ed. Engl.*, 1991, **30**, 1069–1085.
3 N. Fey, *J. Chem. Technol. Biotechnol.*, 1999, **74**, 852–862.
4 H. Werner, *Angew. Chem., Int. Ed.*, 2012, **51**, 6052–6058.
5 T. J. Kealy and P. L. Pauson, *Nature*, 1951, **168**, 1039–1040.
6 S. A. Miller, J. A. Tebboth and J. F. Tremaine, *J. Chem. Soc.*, 1952, 632–635.
7 G. Wilkinson, M. Rosenblum, M. C. Whiting and R. B. Woodward, *J. Am. Chem. Soc.*, 1952, **74**, 2125–2126.
8 E. Fischer and W. Pfab, *Z. Naturforsch., B: J. Chem. Sci.*, 1952, **7**, 377–379.
9 A. Streitwieser Jr and U. Mueller-Westerhoff, *J. Am. Chem. Soc.*, 1968, **90**, 7364.
10 A. Streitwieser Jr and N. Yoshida, *J. Am. Chem. Soc.*, 1969, **91**, 7528.
11 J. Goffart, J. Fuger, D. Brown and G. Duyckaerts, *Inorg. Nucl. Chem. Lett.*, 1974, **10**, 413–419.
12 D. G. Karraker, J. A. Stone, E. R. Jones Jr and N. Edelstein, *J. Am. Chem. Soc.*, 1970, **92**, 4841–4845.
13 A. Avdeef, K. N. Raymond, K. O. Hodgson and A. Zalkin, *Inorg. Chem.*, 1972, **11**, 1083–1088.
14 D. Seyferth, *Organometallics*, 2004, **23**, 3562–3583.
15 J.-C. Berthet, P. Thuéry, N. Garin, J.-P. Dognon, T. Cantat and M. Ephritikhine, *J. Am. Chem. Soc.*, 2013, **135**, 10003–10006.
16 A. Kerridge, R. Coates and N. Kaltsoyannis, *J. Phys. Chem. A*, 2009, **113**, 2896–2905.

17 A. Kerridge, *Dalton Trans.*, 2013, **42**, 16428–16436.
18 A. Streitwieser, S. A. Kinsley, J. T. Rigsbee, I. L. Fragala and E. Ciliberto, *J. Am. Chem. Soc.*, 1985, **107**, 7786–7788.
19 K. N. Raymond and C. W. Eigenbrot, *Acc. Chem. Res.*, 1980, **13**, 276–283.
20 M. Dolg, P. Fulde, H. Stoll, H. Preuss, A. Chang and R. M. Pitzer, *Chem. Phys.*, 1995, **195**, 71–82.
21 M. Dolg and O. Mooßen, *J. Organomet. Chem.*, 2015, **794**, 17–22.
22 I. Grenthe, J. Drożdżyński, T. Fujino, E. C. Buck, T. E. Albrecht-Schmitt and S. F. Wolf, in *Uranium*, ed. L. R. Morss, N. M. Edelstein and J. Fuger, Springer Netherlands, Dordrecht, 2006, pp. 253–698.
23 D. L. Clark, M. P. Neu, W. Runde and D. W. Keogh, in *Uranium and Uranium Compounds*, John Wiley & Sons, Inc., New York, 2000.
24 M. Pepper and B. E. Bursten, *Chem. Rev.*, 1991, **91**, 719–741.
25 T. W. Hayton, *Nat. Chem.*, 2013, **5**, 451–452.
26 T. Arliguie, M. Lance, M. Nierlich, J. Vigner and M. Ephritikhine, *J. Chem. Soc., Chem. Commun.*, 1995, 183–184.
27 D. Gourier, D. Caurant, T. Arliguie and M. Ephritikhine, *J. Am. Chem. Soc.*, 1998, **120**, 6084–6092.
28 J. Li and B. E. Bursten, *J. Am. Chem. Soc.*, 1997, **119**, 9021–9032.
29 *Organometallics of the f-elements: Proceedings of the NATO advanced study institute held at Sogesta, Urbino, Italy*, ed. T. J. Marks and D. J. Fischer, September 11–22, 1978.
30 W. Liu, M. Dolg and P. Fulde, *J. Chem. Phys.*, 1997, **107**, 3584–3591.
31 M. L. Neidig, D. L. Clark and R. L. Martin, *Coord. Chem. Rev.*, 2013, **257**, 394–406.
32 W. W. Lukens, N. M. Edelstein, N. Magnani, T. W. Hayton, S. Fortier and L. A. Seaman, *J. Am. Chem. Soc.*, 2013, **135**, 10742–10754.
33 J. L. Robbins, N. Edelstein, B. Spencer and J. C. Smart, *J. Am. Chem. Soc.*, 1982, **104**, 1882–1893.
34 H. M. McConnell and D. B. Chesnut, *J. Chem. Phys.*, 1958, **28**, 107–117.
35 H. M. McConnell and C. H. Holm, *J. Chem. Phys.*, 1958, **28**, 749.
36 M. F. Rettig and R. S. Drago, *J. Am. Chem. Soc.*, 1969, **91**, 1361–1370.
37 R. Prins, *J. Chem. Phys.*, 1969, **50**, 4804–4809.
38 D. A. Levy and L. E. Orgel, *Mol. Phys.*, 1960, **3**, 583–587.
39 F. H. Köhler and X. Xie, *Magn. Reson. Chem.*, 1997, **35**, 487–492.
40 S. Li, Y. Hamrick, R. Van Zee and W. Weltner Jr, *J. Am. Chem. Soc.*, 1992, **114**, 4433–4434.
41 M. Rudin, J. Fauth, A. Schweiger, R. Ernst, L. Zoller and J. Ammeter, *Mol. Phys.*, 1983, **49**, 1257–1275.
42 F. Aquino, B. Pritchard and J. Autschbach, *J. Chem. Theory Comput.*, 2012, **8**, 598–609.
43 P. Verma and J. Autschbach, *J. Chem. Theory Comput.*, 2013, **9**, 1932–1948.
44 K. Sharkas, B. Pritchard and J. Autschbach, *J. Chem. Theory Comput.*, 2015, **11**, 538–549.
45 F. Gendron and J. Autschbach, *J. Chem. Theory Comput.*, 2016, **12**, 5309–5321.
46 J. Novotný, D. Prichystal, M. Sojka, S. Komorovsky, M. Necas and R. Marek, *Inorg. Chem.*, 2018, **57**, 641–652.
47 A. V. Arbuznikov, J. Vaara and M. Kaupp, *J. Chem. Phys.*, 2004, **120**, 2127–2139.
48 C. Remenyi, R. Reviakine, A. V. Abuznikov, J. Vaara and M. Kaupp, *J. Phys. Chem. A*, 2004, **108**, 5026–5033.
49 Z.-F. Xu, Y. Xie, W.-L. Feng and H. F. Schaefer, *J. Phys. Chem. A*, 2003, **107**, 2716–2729.
50 P. Hrobárik, R. Reviakine, A. V. Arbuznikov, O. L. Malkina, V. G. Malkin, F. H. Köhler and M. Kaupp, *J. Chem. Phys.*, 2007, **126**, 024107–024119.
51 B. Martin and J. Autschbach, *Phys. Chem. Chem. Phys.*, 2016, **18**, 21051–21068.
52 S. Awais Rouf, J. Mares and J. Vaara, *J. Chem. Theory Comput.*, 2017, **13**, 3731–3745.
53 E. J. Baerends, T. Ziegler, J. Autschbach, D. Bashford, A. Bérces, F. M. Bickelhaupt, C. Bo, P. M. Boerrigter, L. Cavallo, D. P. Chong, L. Deng, R. M. Dickson, D. E. Ellis, M. van Faassen, L. Fan, T. H. Fischer, C. Fonseca Guerra, A. Ghysels, A. Giammona, S. J. A. van Gisbergen, A. W. Götz, J. A. Groeneveld, O. V. Gritsenko, M. Grüning, S. Gusarov, F. E. Harris, P. van den Hoek, C. R. Jacob, H. Jacobsen, L. Jensen, J. W. Kaminski, G. van Kessel, F. Kootstra, A. Kovalenko, M. V. Krykunov, E. van Lenthe, D. A. McCormack, A. Michalak, M. Mitoraj, J. Neugebauer, V. P. Nicu, L. Noodleman, V. P. Osinga, S. Patchkovskii, P. H. T. Philipsen, D. Post, C. C. Pye, W. Ravenek, J. I. Rodríguez, P. Ros, P. R. T. Schipper, G. Schreckenbach, J. S. Seldenthuis, M. Seth, J. G. Snijders, M. Solà, M. Swart, D. Swerhone, G. te Velde, P. Vernooijs, L. Versluis, L. Visscher, O. Visser, F. Wang, T. A. Wesolowski, E. M. van Wezenbeek, G. Wiesenekker, S. K. Wolff, T. K. Woo and A. L. Yakovlev, *Amsterdam Density Functional, Version 2014, SCM, Theoretical Chemistry*, Vrije Universiteit, Amsterdam, The Netherlands, 2014, http://www.scm.com, accessed 08/17.
54 E. van Lenthe, E. J. Baerends and J. G. Snijders, *J. Chem. Phys.*, 1993, **99**, 4597–4610.
55 A. D. Becke, *Phys. Rev. A*, 1988, **38**, 3098–3100.
56 J. P. Perdew, *Phys. Rev. B*, 1986, **33**, 8822–8824.
57 J. P. Perdew, K. Burke and M. Ernzerhof, *Phys. Rev. Lett.*, 1996, **77**, 3865–3868.
58 J. P. Perdew, K. Burke and M. Ernzerhof, *Phys. Rev. Lett.*, 1997, **78**, 1396.
59 A. D. Becke, *J. Chem. Phys.*, 1993, **98**, 5648–5652.
60 C. Lee, W. Yang and R. G. Parr, *Phys. Rev. B*, 1988, **37**, 785–789.
61 S. H. Vosko, L. Wilk and M. Nusair, *Can. J. Phys.*, 1980, **58**, 1200–1211.
62 M. Ernzerhof and G. E. Scuseria, *J. Chem. Phys.*, 1999, **110**, 5029–5036.
63 C. Adamo and V. Barone, *J. Chem. Phys.*, 1999, **110**, 6158–6170.
64 E. van Lenthe and E. J. Baerends, *J. Comput. Chem.*, 2003, **24**, 1142–1156.

65 E. D. Glendening, C. R. Landis and F. Weinhold, *J. Comput. Chem.*, 2013, **34**, 1429–1437.
66 G. Schreckenbach and T. Ziegler, *J. Phys. Chem. A*, 1997, **101**, 3388–3399.
67 J. Autschbach and B. Pritchard, *Theor. Chem. Acc.*, 2011, **129**, 453–466.
68 J. Autschbach and T. Ziegler, *J. Chem. Phys.*, 2000, **113**, 936–947.
69 J. Autschbach and T. Ziegler, *J. Chem. Phys.*, 2000, **113**, 9410–9418.
70 J. Autschbach, *J. Chem. Phys.*, 2008, **129**, 094105.
71 E. van Lenthe, P. E. S. Wormer and A. van der Avoird, *J. Chem. Phys.*, 1997, **107**, 2488–2498.
72 E. van Lenthe, A. van der Avoird and P. E. S. Wormer, *J. Chem. Phys.*, 1998, **108**, 4783–4796.
73 S. Moncho and J. Autschbach, *J. Chem. Theory Comput.*, 2010, **6**, 223–234.
74 F. Aquilante, J. Autschbach, R. K. Carlson, L. F. Chibotaru, M. G. Delcey, L. D. Vico, I. F. Galván, N. Ferré, L. M. Frutos, L. Gagliardi, M. Garavelli, A. Giussani, C. E. Hoyer, G. L. Manni, H. Lischka, D. Ma, P.-Å. Malmqvist, T. Müller, A. Nenov, M. Olivucci, T. B. Pedersen, D. Peng, F. Plasser, B. Pritchard, M. Reiher, I. Rivalta, I. Schapiro, J. Segarra-Martí, M. Stenrup, D. G. Truhlar, L. Ungur, A. Valentini, S. Vancoillie, V. Veryazov, V. P. Vysotskiy, O. Weingart, F. Zapata and R. Lindh, *J. Comput. Chem.*, 2016, **37**, 506–541.
75 B. O. Roos, P. R. Taylor and P. E. M. Siegbahn, *Chem. Phys.*, 1980, **48**, 157–173.
76 K. Andersson, P.-Å. Malmqvist, B. O. Roos, A. J. Sadlev and K. Wolinski, *J. Phys. Chem.*, 1990, **94**, 5483–5488.
77 M. Douglas and N. M. Kroll, *Ann. Phys.*, 1974, **82**, 89–155.
78 B. A. Hess, *Phys. Rev. A*, 1985, **32**, 756–763.
79 B. A. Hess, *Phys. Rev. A*, 1986, **33**, 3742–3748.
80 A. Wolf, M. Reiher and B. A. Hess, *J. Chem. Phys.*, 2002, **117**, 9215–9226.
81 P.-O. Widmark, P.-Å. Malmqvist and B. O. Roos, *Theor. Chim. Acta*, 1990, **77**, 291–306.
82 B. O. Roos, R. Lindh, P.-Å. Malmqvist, V. Veryazov and P.-O. Widmark, *J. Phys. Chem. A*, 2004, **108**, 2851–2858.
83 B. O. Roos, R. Lindh, P.-Å. Malmqvist, V. Veryazov and P.-O. Widmark, *Chem. Phys. Lett.*, 2005, **409**, 295–299.
84 N. Suaud, R. Ruamps, J.-P. Malrieu and N. Guihéry, *J. Phys. Chem. A*, 2014, **118**, 5876–5884.
85 F. Gendron, K. Sharkas and J. Autschbach, *J. Phys. Chem. Lett.*, 2015, **6**, 2183–2188.
86 P.-Å. Malmqvist, B. O. Roos and B. Schimmelpfennig, *Chem. Phys. Lett.*, 2002, **357**, 230–240.
87 B. A. Heß, C. M. Marian, U. Wahlgren and O. Gropen, *Chem. Phys. Lett.*, 1996, **251**, 365–371.
88 H. Bolvin, *ChemPhysChem*, 2006, **7**, 1575–1589.
89 R. Prins and J. D. W. van Voorst, *J. Chem. Phys.*, 1968, **49**, 4665–4673.
90 S. Evans, M. L. H. Green, B. Jewitt, G. H. King and A. F. Orchard, *J. Chem. Soc., Faraday Trans. 2*, 1974, **70**, 356–376.
91 T. A. Jackson, J. Krzystek, A. Ozarowski, G. B. Wijeratne, B. F. Wicker, D. J. Mindiola and J. Telser, *Organometallics*, 2012, **31**, 8265–8274.
92 J. W. Rabalais, L. O. Werme, T. Bergmark, L. Karlsson, M. Hussain and K. Siegbahn, *J. Chem. Phys.*, 1972, **57**, 1185–1192.
93 J. H. Ammeter and J. D. Swalen, *J. Chem. Phys.*, 1972, **57**, 678–698.
94 H. A. Jahn and E. Teller, *Proc. R. Soc. London, Ser. A*, 1937, **161**, 220–235.
95 I. B. Bersuker, *Chem. Rev.*, 2001, **101**, 1067–1114.
96 J. H. Ammeter, *J. Magn. Reson.*, 1978, **30**, 299–325.
97 B. Pritchard and J. Autschbach, *Inorg. Chem.*, 2012, **51**, 8340–8351.
98 M. Cortijo, C. Viala, T. Reynaldo, L. Favereau, I. Fabing, M. Srebro-Hooper, J. Autschbach, N. Ratel-Ramond, J. Crassous and J. Bonvoisin, *Inorg. Chem.*, 2017, **56**, 4556–4568.
99 J. Autschbach and M. Srebro, *Acc. Chem. Res.*, 2014, **47**, 2592–2602.
100 H. Heise, F. H. Köhler and X. Xie, *J. Magn. Reson.*, 2001, **150**, 198–206.
101 M. F. Rettig and R. S. Drago, *Chem. Commun.*, 1966, 891–892.
102 H. Eicher and F. H. Köhler, *Chem. Phys.*, 1988, **128**, 297–309.
103 N. Hebendanz, F. H. Köhler, F. Scherbaum and B. Schlesinger, *Magn. Reson. Chem.*, 1989, **27**, 798–802.
104 B. R. McGarvey, *Can. J. Chem.*, 1984, **62**, 1349–1355.
105 W. D. Luke and A. Streitweiser, in *Nuclear Magnetic Resonance Studies of Uranocenes*, American Chemical Society, Washington, D. C., 1980, ch. 6, pp. 93–140.
106 K. Pierloot, B. J. Persson and B. O. Roos, *J. Phys. Chem.*, 1995, **99**, 3465–3472.
107 Q. M. Phung, S. Vancoillie and K. Pierloot, *J. Chem. Theory Comput.*, 2012, **8**, 883–892.
108 F. Gendron, B. Pritchard, H. Bolvin and J. Autschbach, *Dalton Trans.*, 2015, **44**, 19886–19900.
109 C. J. Stein, V. von Burg and M. Reiher, *J. Chem. Theory Comput.*, 2016, **12**, 3764–3773.
110 A. Kerridge and N. Kaltsoyannis, *J. Phys. Chem. A*, 2009, **113**, 8737–8745.
111 A. Kerridge, *RSC Adv.*, 2014, **4**, 12078–12086.
112 R. Prins, J. D. W. Van Voorst and C. J. Schinkel, *Chem. Phys. Lett.*, 1967, **1**, 54–55.
113 P. Baltzer, A. Furrer, J. Hulliger and A. Stebler, *Inorg. Chem.*, 1988, **27**, 1543–1548.
114 F. Gendron, D. Páez-Hernández, F.-P. Notter, B. Pritchard, H. Bolvin and J. Autschbach, *Chem.–Eur J.*, 2014, **20**, 7994–8011.
115 J. Autschbach, *Comments Inorg. Chem.*, 2016, **36**, 215–244.
116 J. Hulliger, L. Zoller and J. H. Ammeter, *J. Magn. Reson.*, 1982, **48**, 512–518.